

Characteristics of parallel electric fields in the downward current region of the aurora

L. Andersson^{a)}

The Laboratory for Atmospheric and Space Physics, University of Colorado, Boulder, Colorado 80309

R. E. Ergun

The Laboratory for Atmospheric and Space Physics, University of Colorado, Boulder, Colorado 80309

and The Department of Astrophysical and Planetary Sciences, University of Colorado, Boulder,

Colorado 80309

D. L. Newman

Center for Integrated Plasma Studies, University of Colorado, Boulder, Colorado 80309

J. P. McFadden and C. W. Carlson

Space Science Laboratory, University of California, Berkeley, California 94720

Y.-J. Su

The Laboratory for Atmospheric and Space Physics, University of Colorado, Boulder, Colorado 80309

(Received 19 December 2001; accepted 7 May 2002)

Direct measurements of parallel electric fields suggest that they are, in part, self-consistently supported as strong double layers in the auroral downward current region. The observed parallel electric fields have amplitudes reaching nearly 1 V/m and are confined to a thin layer of approximately 10 Debye lengths. The structures are moving at roughly the ion acoustic speed in the direction of the accelerated electrons, i.e., anti-earthward. On the high-potential side of the parallel electric field there is a clear signature of an accelerated electron beam which rapidly plateaus within a few hundred Debye lengths from the parallel electric field. Strong wave turbulence is observed in the vicinity of the plateaued electron distribution. Fast solitary waves, identified as a signature of electron phase-space holes, are seen farther away from the parallel electric field on the high-potential side. The observed ion distributions also indicate the presence of the parallel electric field. On the low-potential side of the double layer an ion beam is observed moving in the opposite direction of the electron beam and ion conics appear to be trapped between their mirror point and the moving double layer. © 2002 American Institute of Physics. [DOI: 10.1063/1.1490134]

I. INTRODUCTION

The auroral downward current region has only recently been identified as a dynamical entity. In early observations of this region, anti-earthward, field-aligned electron beams were detected sporadically by several auroral satellites; for instance, International Satellites for Ionospheric Studies-2,¹ Dynamics Explorer-1,² Viking,³ Freja,⁴ and Akebono.⁵ Counter streaming electrons^{6,7} were also observed. Fast Auroral SnapshoT (FAST) observations^{8,9} establish that anti-earthward field-aligned beams are common auroral features that are associated with diverging electric field structures,^{8,13} and provided strong evidence that the anti-earthward field-aligned electron beams are energized by parallel electric fields.¹⁴ The upward electron beams are often accompanied by ion conics.^{3,5,10} In this region, precipitating ion beams also have been found.^{11,12} The field-aligned current-voltage relationship for the downward current region, however, is clearly nonlinear,¹⁵ and the presence of upward accelerated electron beams depends on the ionospheric scale height.¹⁶

Even though parallel electric fields have been postulated in the auroral region for many years, they have eluded direct

observation and, thus, a self-consistent structure has not been identified. From early electric field observations, small amplitude double layers have been reported.^{17,18} Recently, however, stronger parallel electric fields have been directly measured in both the upward¹⁹ and downward current regions.¹² The downward current region observations indicate structures corresponding to strong double layers, with a substantial turbulent region on the high-potential side.²⁰

Double layers have been studied, for instance, in laboratory experiments and in numerical simulations.^{21–23} Monotonic double layers can be analytically described.²⁴ The non-linear evolution of double layers, however, has been studied primarily in numerical simulations. The double layers in the simulations are typically created by an electron beam in a plasma or in a plasma with fix potential drop at the boundaries.

Following the observation of fast solitary waves in space plasmas,^{25–29} simulations have been performed to explain the origin of these electron phase-space holes. These periodic simulations start with a strong current or electron beam and are unstable to the two-stream instability.^{30–33} The presence of a background density gradient in such simulations can be important.³⁴ The observations of parallel electric fields¹²

^{a)}Electronic mail: andersson@lasp.colorado.edu

from FAST mission and simulations³⁵ now show that, within a current driven plasma, electron phase-space holes can evolve together with a double layer. Our observations indicate that the intense wave turbulence associated with the electron phase-space holes does not destroy the double layer. The double layer creates an electron beam which in turn creates electron phase-space holes.

In this paper, we present FAST satellite observations of parallel electric fields and associated turbulence in the downward current region. These observations, which are possible due to FAST's orbital characteristics and high time resolution instrumentation, provide direct evidence for the structure of the acceleration process in these regions. We focus on an event which is recorded with the FAST satellite's highest time resolution. We show the following:

- (i) the parallel electric field structure in the downward current region is consistent with that of a strong double layer;
- (ii) the potential structure can accelerate electrons to several times the parallel electron thermal energy;
- (iii) the extent of the potential drop parallel along the magnetic field is of the order of 10 Debye lengths;^{17,12}
- (iv) the double layer is moving at the ion acoustic speed anti-earthward along the magnetic field, i.e., in the same direction of the accelerated/streaming electrons.

The particle acceleration takes place in a quasistatic structure, with no apparent co-located wave activity. Intense wave turbulence, however, is found on the high-potential side of the double layer. In this turbulent region, the accelerated electron beam is rapidly heated and plateaued, with wave-particle interactions playing an important role in the relaxation of the electron beam. Far from the double layer (hundreds of Debye lengths away), isolated electron phase-space holes are observed to emerge from the turbulent region.

The double layer also effects the ions significantly. In particular, it constrains the upward motion of the ion conics that originate on the low-potential side; accelerates ions that originate on the high-potential side into a beam-like structure in the opposite direction of the electron beam.

This paper is organized as follows. Details of the particle and field observations are presented in Sec. II. The dc electric fields are analyzed in Sec. III and the wave turbulence in Sec. IV. The measurements are compared with numerical simulations in Sec. V. The significance of this event is discussed in Sec. VI followed by a summary in Sec. VII.

II. EVENT DESCRIPTION

The event presented here is a rare but particularly interesting observation of a parallel electric field in the auroral downward current region. The maximum field amplitude was ~ 850 mV/m from which an accelerated upward electron beam emerges with a peak energy of ~ 750 eV. One similar case has been reported earlier,¹² however, the satellite was configured to observe at a substantially lower time resolution compared to the current event. Out of over 300 upward electron beams resolved at high time resolution, this is the only

case where a verifiable large-amplitude parallel electric field has been identified (the analyzed time period is mainly at solar minimum, 1997). Few observations are expected since the limited extent of the parallel electric fields make the probability of detecting them low. To detect both the upward accelerated electrons and the parallel electric field using a satellite can only be done if there is a relative motion, in the direction of the magnetic field, between the satellite and the electric field structure.

The event shown in Fig. 1 took place on 7 January 1998 between 13:12:47.4 and 47.9 UT. Over this 0.5 second period the spacecraft moved 700 m vertically and 3.3 km horizontally. The observation was made at 21.9 MLT, at an altitude of 2470 km and an invariant latitude of 73.0 degrees. At the beginning of the event (47.4 UT) the FAST satellite detected a weak upward electron beam with a mean energy of 75 eV. At the end of the event (47.9 UT) the satellite again detected a weak, 50 eV upward electron beam. Ion conics were observed both before and after the encounter of the parallel electric field. The magnetic field strength is $|\mathbf{B}| = 22\,085$ nT. (Detailed instrument description and information about the FAST mission can be found in Ref. 37.)

Panel (a) of Fig. 1 presents an energy-time spectrogram of the anti-earthward (upward) electron flux (within $\pm 22.5^\circ$ of $-\mathbf{B}$) measured by a swept-energy electron electrostatic analyzer (EESA). Each energy sweep is completed in ~ 79 ms by an instrument that has an opening aperture of $11.2 \times 10^\circ$. The energy sweep (high to low energies) is approximately a pseudoexponential sweep that passes the energy of 1 keV about 1/3 of the way through the sweep. Four of the energy sweeps will be referred to as S1 to S4, as indicated above panel (a). Panel (b) plots the count rates of upward, field-aligned electrons (the detector closest to $-\mathbf{B}$) from fixed-energy electron electrostatic analyzers (SESAs). The SESAs have a time resolution of ~ 1.63 ms and an opening aperture of $22.5 \times 10^\circ$. The black and red lines represent the fixed-energy channels of 700 eV and 1.3 keV, respectively. The energy acceptance (dE/E) of the EESAs on FAST³⁸ is 0.15. We refer only to the center energy in the text.

Panel (c) presents the component of the perpendicular electric field (\mathbf{E}_\perp) in the plane of the satellite motion. Negative values represent electric fields approximately opposite to the motion of the spacecraft. The black and red line represent the $f < 16$ kHz and $f < 200$ Hz filtered (dc) signals, respectively. In panel (d), the parallel electric field (\mathbf{E}_\parallel) is presented, where both 16 kHz and the 200 Hz lines are again represented by the black and red lines. The large-amplitude signal (~ 0.85 V/m) in the \mathbf{E}_\parallel between 47.75 UT and 47.79 UT stands out in panel (d) and is referred to as the \mathbf{E}_\parallel structure. Interestingly, there is very little wave activity concurrent with that \mathbf{E}_\parallel structure. A fast Fourier transform (FFT) of the \mathbf{E}_\perp signal from panel (c) is presented in panel (e). Panel (f) shows the potential difference from the integration of the \mathbf{E}_\perp (blue line), the \mathbf{E}_\parallel (red line), and a combination of the two (black line). The spacecraft velocity for this event was 6.62 km/s (mainly horizontal) and the \mathbf{E}_\parallel structure is assumed to move up along the field line with a velocity of 36 km/s (which will be justified later in the paper).

Electron and ion distributions, from the EESA and IESA

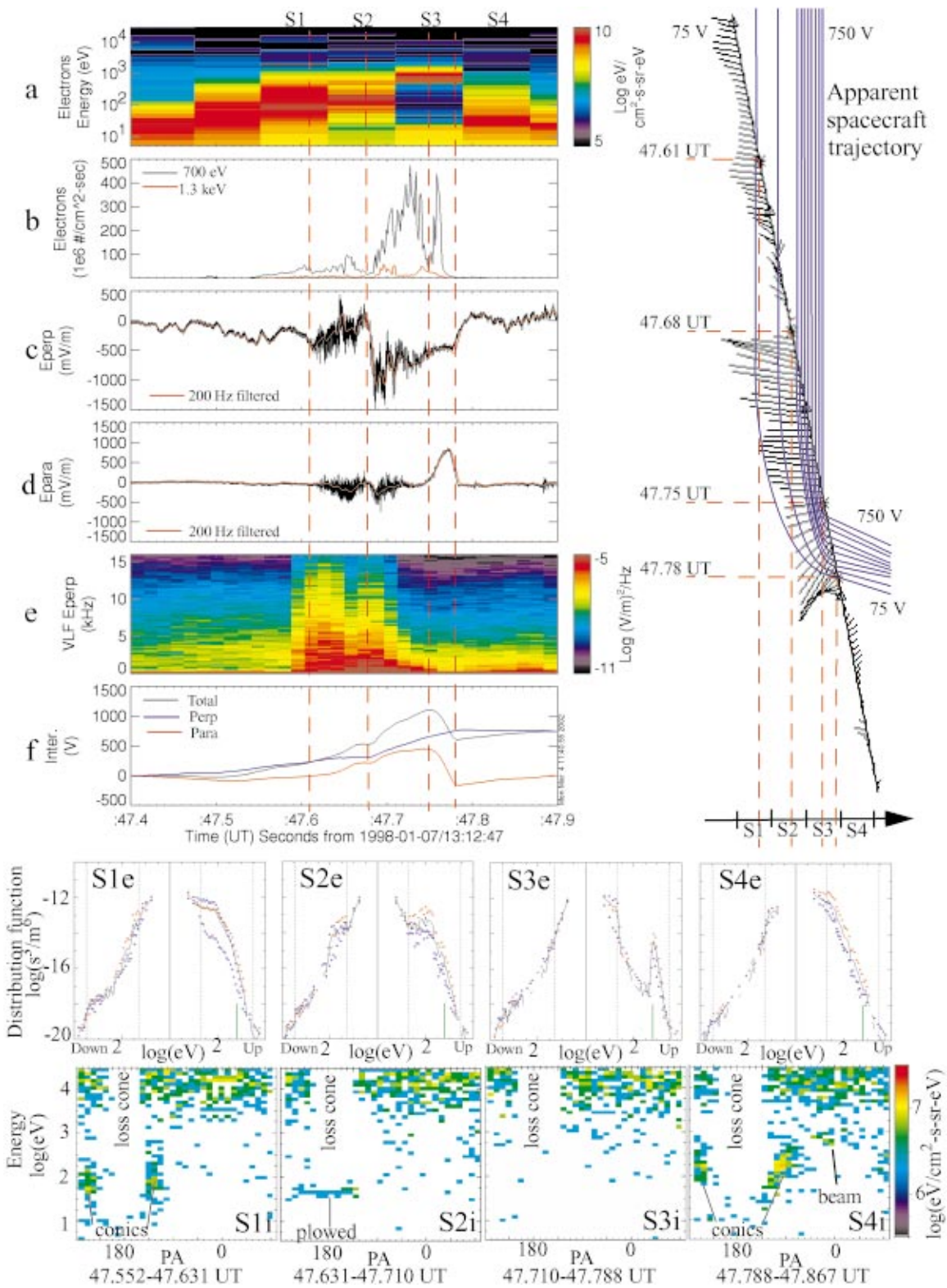


FIG. 1. (Color) The field and particle observations of the half second event.

(ions), from energy sweep S1–S4 are plotted at the bottom of Fig. 1, labeled S1e–S4e and S1i–S4i, respectively. The distributions, S1e–S4e, show the electron phase-space density [$\log(\text{s}^3/\text{m}^6)$] as a function of electron energy [$\log(\text{eV})$], where the left and right distributions are for earthward and anti-earthward (downward and upward) electrons, respec-

tively. The solid line represents the mean electron distribution, within ± 22.5 degrees of the $-\mathbf{B}$. The red and blue dotted lines are the three most field-aligned electron distributions which are, for all panels, centered at $3, 9,$ and 14 ± 2 degrees from the $-\mathbf{B}$, where the red dotted line represents the most field-aligned sector at the time half way

through the energy sweep (i.e., it is not necessarily the most field-aligned at start or end of the sweep). The electron distribution is highly anisotropic with the highest fluxes along the $\pm \mathbf{B}$ direction. The perpendicular temperature is less than 1 eV and the parallel electron temperature is in the range of 20 to 100 eV (using the 20 eV to 3 keV particle detector energy range). In the electron distribution plots (Fig. 1 sweep S1e–S4e), the dotted vertical lines indicate ± 20 eV and ± 3 keV energies, and the short green line indicates 650 eV upward electrons. The electron distribution below 20 eV may be contaminated by spacecraft-originated photoelectrons.

At the bottom of Fig. 1, the ion distributions (S1i–S4i) are plotted as functions of energy (vertical axis) and pitch angle (horizontal axis). The ion conics in S1i and S4i have energies from about 80 eV up to 800 eV. The conic angles of sweep S1i are in between 90° and the loss cone with the same pitch angle for all energies. The ion conic in sweep S4i has pitch angles that are closer to 90° with increasing energy.

The particle detectors (ions and electrons) and a Langmuir probe (not shown) indicate that the density before 47.61 UT was $\sim 15 \times 10^6 \text{ m}^{-3}$ (sweep S1) and after 47.78 UT was $\sim 10 \times 10^6 \text{ m}^{-3}$ (sweep S4). Between 47.61 UT and 47.71 UT (the time period of sweep S2), the Langmuir probe measurements were not valid due to high wave activities. The Langmuir probe between 47.71 UT and 47.78 UT (the time period of sweep S3) indicates low current, that is, below the instrument resolution. We interpret the low current as a density depletion since there was no wave activity. This interpretation is supported by particle distributions. The electron and ion sweeps S3 indicate a density of $1\text{--}2 \times 10^6 \text{ m}^{-3}$ (in contrast to the sweep S2 that has a density of $\sim 5 \times 10^6 \text{ m}^{-3}$). The density estimations, both from the particle distributions and the probe, have similar uncertainty of a factor of 2. The ions below 1 keV are assumed to contain 20% oxygen (the rest of protons), for an agreement between electron and ion densities.

On the upper right hand of Fig. 1, an illustration is presented of a possible electric field structure that the satellite passed through. It will be described later. Much of the discussion will be keyed to the specific times of 47.61 UT, 47.68 UT, 47.75 UT, and 47.78 UT, which are indicated by red dashed lines in panels (a)–(f) and on the illustration (Fig. 1).

III. THE DC ELECTRIC FIELD

As shown in Fig. 1(c), \mathbf{E}_\perp is mainly negative during the in-bound part of the event (47.61 UT to 47.78 UT). Using the speed of the satellite, the integrated electric field indicates that the satellite moved from a lower potential (47.61 UT) to a higher potential (47.75 UT), seen as the blue line in Fig. 1(f). The potential difference is about 800 V, which is also equal to the change of the particle energy of the upward electron beam^{9,14} [panel (a)]. We therefore interpret the \mathbf{E}_\perp signal as the entry of a diverging potential structure.

The exit from the diverging potential structure was not detected in \mathbf{E}_\perp . Instead, there is a clear electric field signature in \mathbf{E}_\parallel between 47.75 UT and 47.78 UT [Fig. 1(d)]. We conclude that the measured \mathbf{E}_\parallel structure is the electric field at

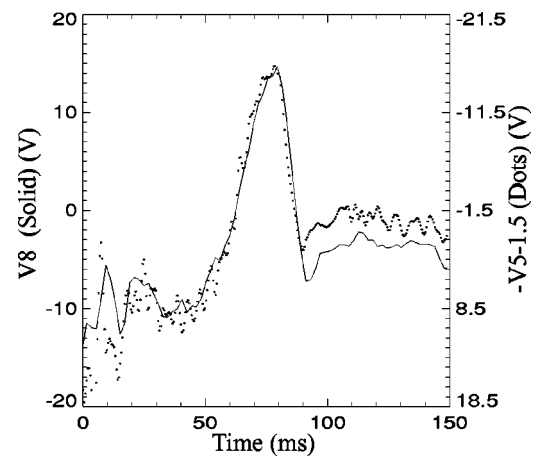


FIG. 2. The potential on probe 8 (solid line) and 5 (dotted line) between 47.70 UT and 47.95 UT. Probes 8 and 5 are the two most magnetic field-aligned probes, where probe 5 is the most earthward one.

the bottom of a diverging potential structure and that the satellite leaves the potential structure through the region dominated by \mathbf{E}_\parallel .

To estimate the potential across the \mathbf{E}_\parallel structure, the relative velocity between the satellite and the \mathbf{E}_\parallel structure needs to be determined. The relative velocity can be estimated by analyzing the delay time between spatially separated probes as they detected the electric field structure. In Fig. 2, the electric field measurements from the two most field-aligned probes are presented. The most earthward probe, probe 5, detected the structure first, indicating an upward velocity of the structure. The delay times between the two probes are small, at the edge of being resolvable. From this delay time, the upward velocity lies in the interval of $53 + 53 / - 26 \text{ km/s}$. The delays are inconsistent with significant velocity perpendicular to \mathbf{B} .

A speed of 36 km/s (which is consistent with the measured delay) yields an integrated \mathbf{E}_\parallel between 47.75 UT and 47.78 UT of 800 V [Fig. 1(f) red line], which is equal to the in-bound potential difference determined from the integrated \mathbf{E}_\perp . The measured \mathbf{E}_\parallel is highly uncertain during times of strong wave turbulence since the probes might have experienced ac saturation. The \mathbf{E}_\parallel also may have a small ($< 10 \text{ mV/m}$) zero offset, so integration over long periods may accumulate error [Fig. 1(f) red line]. These uncertainties also apply to the total integrated electric field (\mathbf{E}_\parallel and \mathbf{E}_\perp combined) shown as the black line in panel (f).

Figure 3 presents an interpretation of the SESA observations. The top panel of Fig. 3 is an expanded view of Fig. 1(b). The flux of 1.3 keV electrons is enhanced by a factor of 2 to make the trace more readable. The bottom panels of Fig. 3 depict velocity distributions [labeled (b)–(g) in order of decreasing time] that illustrate a possible evolution of the electron beam peak consistent with those two energy channels. After 47.78 UT [Fig. 3(b)], the peak of velocity distribution is well below the 700 eV channel of the SESA detector. As the electrons enter the \mathbf{E}_\parallel structure the electron distribution peak moves to higher energies [Fig. 3(c)] causing a large increase in the flux at 700 eV. Within the \mathbf{E}_\parallel structure [Fig. 3(d)], the 700 eV flux drops which indicates

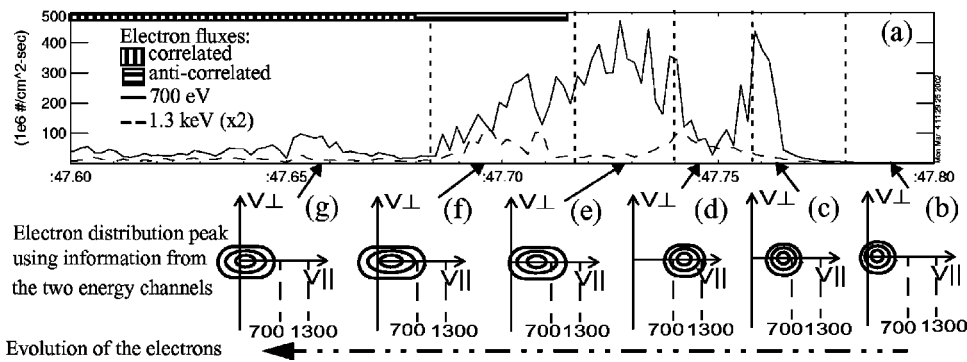


FIG. 3. An interpretation of the measured SESA electron fluxes. Regions where the 700 eV and 1.3 keV SESA are correlated and anticorrelated are indicated.

that the electron distribution peak has passed to energies above 700 eV. The count rates in the 1.3 keV channel continue to increase throughout the E_{\parallel} structure indicating that the electron distribution peak never reaches 1.3 keV. As the electron distribution peak passes 700 eV, the flux level start to fluctuate, suggesting an onset of an instability. Once the electrons have passed through the E_{\parallel} structure (47.75 UT), the flux rate in the 700 eV channel slowly starts to increase again. This increase in the 700 eV fluxes indicates that the electron distribution peak moves back to lower energies. The peak declines through 700 eV as illustrated in Figs. 3(e) and 3(f). At ~ 47.68 UT [Fig. 3(g)] the two SESA channels detect significant lower fluxes indicating that the electron distribution peak is well below 700 eV.

The SESA observations can be compared to the measurements from the EESA. Starting on the right-hand side of Fig. 1, the electrons have low temperatures and low drift velocities as evident in electron distribution S4e. As the electrons enter the E_{\parallel} structure (between 47.75 UT and 47.78 UT, part of sweep S3e), the electrons are accelerated. The distribution S3e shows a clear large peak at and above energy 650 eV (the green short solid line in the bottom of the distribution). The particle fluxes for energies above 650 eV are all measured prior to 47.75 UT, i.e., outside the E_{\parallel} structure on the high-potential side. As the electron beam becomes unstable, wave-particle interactions take place. The electron beam is plateaued as shown in distribution S2e. The wave-particle interaction slows down when the distribution is almost stable, sweep S1e.

The ion distributions are also consistent with a moving E_{\parallel} structure that carries a total integrated potential of ~ 800 V. A downward 800–1300 eV ion beam is seen in sweep S4i (pitch angle of $0^{\circ}/360^{\circ}$) and in the next sweep (Fig. 4). This downward beam is ions accelerated through the potential drop and represents the counterpart to the electron beam. The ion beam is broader in pitch angle than its counterpart, the electron beam. Because of the low ion fluxes, the detected count rates are low and the ion beam is not well resolved.

Within the E_{\parallel} structure, sweep S3i, the ion fluxes are weak except for the precipitating high energy plasma sheet ions. During sweep S2i no ion conic population is detected, however, within the loss cone, a high flux of upward ions (pitch angle centered at 180°) is seen at a narrow energy between 80 and 100 eV. These upward ions have a speed of ~ 36 km/s if assumed to be O^{+} . This speed is identical to the speed of the E_{\parallel} structure that was determined from the inte-

gration of the E_{\parallel} [Fig. 1(f)]. This speed is also, within uncertainties, the local ion acoustic speed. In the reference frame of the E_{\parallel} structure (speed of 36 km/s) the upward ions have a energy width in the parallel direction of 5 eV. These upward ions is measured during a strong $E_{\perp} \times B$ drift. The best interpretation of these upward ions are a oxygen population that is drifting with the $E_{\perp} \times B$ drift perpendicular to the fan instrument and move up the field line with 36 km/s. The oxygen population is cool in the parallel direction but warm, much larger than 50 eV, in the perpendicular direction.

The electric field, electron, and ion observations are consistent with the satellite encountering a diverging electric field as illustrated on the right-hand side of Fig. 1. In the illustration, the apparent satellite path (black line) is drawn in the reference frame of the E_{\parallel} structure. The satellite has a relative horizontal velocity of 6.2 km/s and a vertical velocity of 36 km/s with respect to the E_{\parallel} structure. The electric field relative strength and the direction of the electric field are drawn on top of the satellite path spaced at equal distances. Contour lines, drawn in blue, represent a possible potential structure.

The electron measurements imply that the satellite moves from a potential of ~ 75 V into a potential >750 V with respect to the ionosphere. The integrated E_{\perp} supports the same potential difference. The spacecraft exits the potential structure passing through the region of strong E_{\parallel} in the bottom of the structure. The speed of the E_{\parallel} structure calculated from the delay times of electric field signature has a

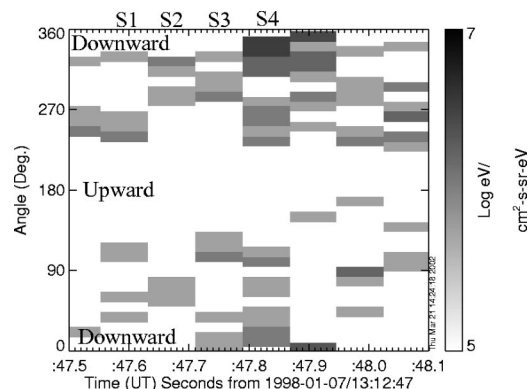


FIG. 4. The particle flux for the ions in energy interval 700 eV to 1.2 keV as a pitch angle versus time spectrogram. At the time of sweep 4 and the next sweep, a downward ion beam detected (0° and 360°) is one order of magnitude larger than elsewhere.

TABLE I. The E_{\parallel} structure (47.75–47.79 UT).

| Properties | Value | Supported by | Comment |
|---------------------|---------------------|---|---------------------------|
| Thickness | $\sim 10\lambda_D$ | Observations and simulations | Using density from S3 |
| Velocity | 53+53/ -26 km/s | ~ 36 km/s from the ions, electrons and E-fields | \sim ion acoustic speed |
| Potential | ~ 800 V | E-fields, electrons and ions | |
| e -drift increase | 4–5 times the v_e | Electrons and simulation | |
| Density depletion | ~ 80 – 90 % | Electrons, ions, Langmuir probe and simulation | |

large uncertainty. However, the speed of the structure estimated from equating the integrated E_{\perp} and E_{\parallel} , the speed estimated by comparing the integrated potential with the energies of the observed electron and ion beams, the speed of the upward ions in front of the E_{\parallel} structure and the calculated local ion acoustic speed are all, within uncertainties, equal. All together, the observations, directly or indirectly support that the velocity of the E_{\parallel} structure should be ~ 36 km/s. The properties of the E_{\parallel} structure are summarized in Table I.

IV. THE HIGH FREQUENCY ELECTRIC FIELD FLUCTUATIONS

Intense electrostatic waves are evident in Fig. 1(e) between 47.61 UT and 47.75 UT. A close examination shows that there were two periods of intense emissions separated by

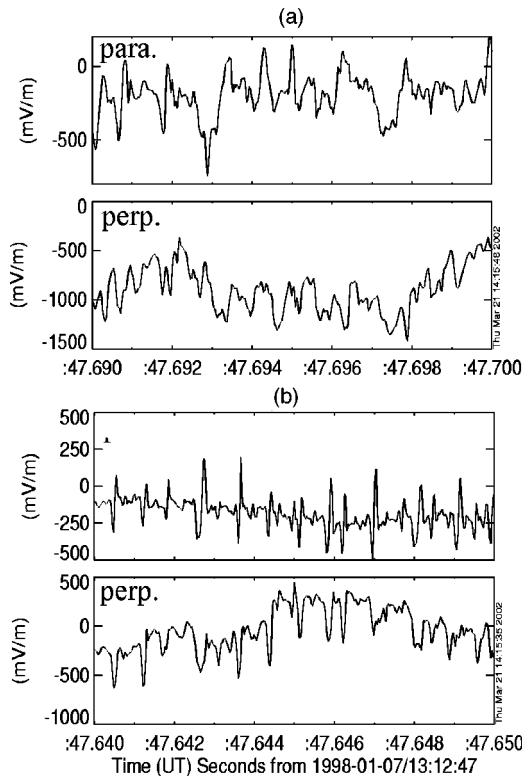


FIG. 5. The parallel (para) and the perpendicular (perp) electric field signatures of the two different wave regions (time period length is 0.01 seconds). Case (a) shows the broadband electrostatic turbulence region (47.69–47.70 UT) and case (b) shows electron phase-space holes (47.64–47.65 UT). Some clipping of the signal might occur.

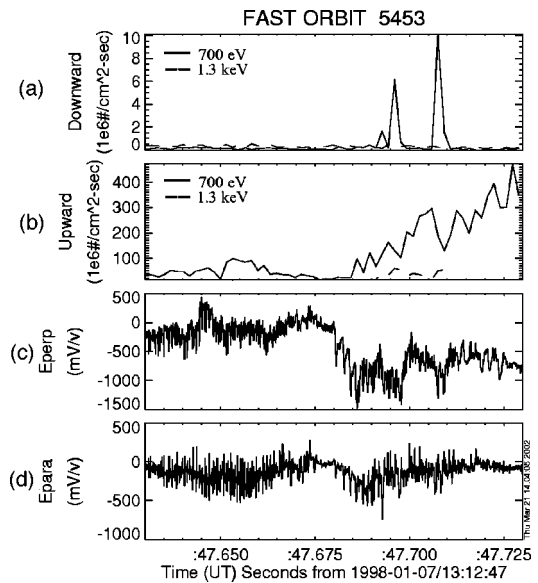


FIG. 6. Data from a 0.1 second period, that contains sweep S2e, indicate wave-particle interactions. The top panels (a) and (b) show the count rates for the downward and the upward flux for energy 700 eV (solid line) and 1.3 keV (dashed line) measured by the SESA. The bottom panels (c) and (d) are the perpendicular and the parallel electric field (16 kHz filtered).

a minima in the wave activity at 47.68 UT [Figs. 1(c), 1(d), and 1(e)]. It is possible that the minima in the wave activity can be due to the satellite’s motion from one flux tube into another. Regardless of the interpretation of the minima, the two periods of intense wave activities have different characteristics. Snapshots of the wave forms are displayed in Fig. 5. The wave emissions closer to the E_{\parallel} structure (~ 47.70 UT) have no identifiable structure and can only be identified as broadband electrostatic turbulence [Fig. 5(a)]. The emissions farther from the E_{\parallel} [between 47.61 UT and 47.68 UT, Fig. 5(b)] show the characteristic signature of electron phase-space holes. Large-amplitude bipolar signals are detected in E_{\parallel} concurrently with a unipolar signal in E_{\perp} . The amplitudes of the measurements indicate a possible saturation of the instrument in both Figs. 5(a) and 5(b) (the instrument limit is about 300 mV/m at this frequency), hence, some clipping of the wave signatures might occur and the true shape of the waves might not be recorded in Fig. 5.

The electron phase-space holes are irregularly spaced with an occurrence frequency of about 1 every millisecond [Fig. 5(b)]. They have an electric field signature of up to about 600 mV/m (or more) peak-to-peak value and a duration of about 150 microseconds. The electron phase-space holes are detected far away from the E_{\parallel} structure between 47.61 UT and 47.68 UT.

Electron phase-space holes can interact strongly with electrons.²⁸ Direct evidence for such an interaction is seen only occasionally during this event. An expanded view of the electron fluxes and electric field are presented in Fig. 6, which includes the downward [panel (a)] and upward [panel (b)] electron fluxes at energies of 700 eV and 1.3 keV from the SESA channels. Panels (c) and (d) show the high-frequency E_{\parallel} and E_{\perp} , respectively. The selected time period covers sweep S2e. At 47.718 UT (Fig. 6), the upward 700 eV

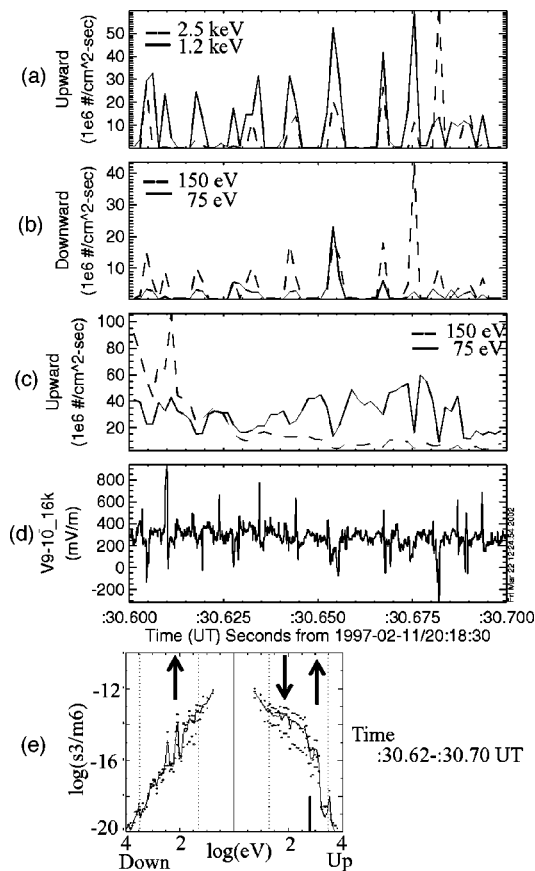


FIG. 7. Similar to Fig. 6 but from another orbit, 1997-02-11/20:18:30.6 UT (again 0.1 second long). The top three panels are upward and downward count rates from the SESA of energies 0.075, 0.15, 1.2, and 2.5 keV. Panel (d) is the 16 kHz electric field measurements from one probe pair. Panel (e) shows the associated electron distribution with the same layout as for sweeps S1e–S4e in Fig. 1.

SESA flux decrease [panel (b) solid line], while the upward 1.3 keV SESA [panel (b) dashed line] and the downward 700 eV SESA [panel (a) solid line] fluxes increase.

The wave–particle interaction associated with electron phase-space holes is illustrated in more detail from another orbit (Fig. 7) where the SESA measured in a lower energy range. Measurements from 75, 150, 1200, and 2500 eV energies are displayed for both up [panels (a) and (c)] and downward [panel (b)] electron fluxes. The perpendicular electric field from the probe pair, 9 and 10, is plotted in panel (d). (This signal is from a short baseline dipole and thus has a saturation level >2 V/m.) In this example, the fluctuations in the electron fluxes directly correspond to the large-amplitude signals in the electric field. The time resolution of the electron fluxes (~ 1.63 ms) differs dramatically from that of the electric field signal (0.030 ms), so the fluctuations in the electron fluxes appear broader.

The electron distribution measured by the EESA for the same time period is plotted at the bottom of Fig. 7 in panel (e). The distribution shows a net upward flux with the peak energy of the distribution in the energy range of 100 to 200 eV. The large fluctuations in the SESA electron fluxes [panels (a) and (b)] are correlated with the electric field signals [panel (d)]. From the normal fluxes one can see that the

count rates decrease for the upward 75 and 150 eV electron fluxes [panel (c)], while the count rates increases for the downward energies 75 and 150 eV and the upward energies 1.2 and 2.5 keV [panels (b) and (a), respectively]. The changes in flux levels are indicated with arrows in the electron distribution of panel (e). These changes in flux levels are expected from strong wave–particle interaction within an electron phase-space hole. Clear changes in the electron fluxes are seen at energies ~ 75 eV downward and ~ 150 eV and ~ 1.2 keV upward. At the energies in between—the transition region between enhanced and decreased fluxes—no significant changes in the flux levels are seen.

At the time period of Fig. 3(d), the peak energy of the electron distribution is high and therefore the 1.3 keV SESA channel measuring high fluxes. As the energy peak in the electron distribution decreases, the flux of the 1.3 keV SESA channel also decreases [Fig. 3(e)]. The flux levels in the 1.3 keV SESA channel increases again due to wave interactions shown in Fig. 7. At the time of Fig. 3(f), the peak energy of the electron distribution is below 700 eV, but the decrease of flux [shown in Fig. 7(c)] still can be observed by the 700 eV SESA channel and the increase of flux at high energies [shown in Fig. 7(a)] can be observed by the 1.3 keV SESA channel. During Fig. 3(f) the flux levels are anticorrelated, as seen in Fig. 3(a). When the peak energy of the electron distribution is well below 700 eV [Fig. 3(g)], the 700 eV SESA channel is no longer measuring the decrease of the flux but instead the increase of the flux [equal to Fig. 7(a)]. During Fig. 3(g) the flux levels are correlated, as seen in Fig. 3(a). The reason the 1.3 keV SESA channel do not see any flux changes for the time period of Fig. 3(e), is that the channel is measuring in the transition region (see Sec. III). How the flux for each energy range fluctuates depends on where the peak energy of the distribution is.

The observed wave–particle interactions²⁸ lead to the plateauing of the electron beam. In the reference frame of the beam, some of the electrons will be accelerated downward and others upward, so in the frame of the spacecraft, some particles will have lower energies and other higher energies. The total energy flux is nearly conserved, with kinetic energy flux transferred to thermal energy flux through heating of the plasma. The result of this wave–particle interaction—the plateauing of the electron beam—is seen in distribution S2e and the distribution of Fig. 7(e), where the particle distribution has two shoulders; one shoulder is the remnant of the beam and the other is the electrons from the beam that have been reflected and/or accelerated in the opposite direction of the beam. Those of the electrons that gain energy in the wave–particle interaction form the high energy tail of the electron distribution.

V. COMPARISON WITH NUMERICAL SIMULATIONS

Numerical simulation using a 1D, open boundary Vlasov code^{35,36} were used to analyze a previously reported E_{\parallel} observation in the downward current region.¹² Figure 8(a) displays the results of a plasma simulation that started with a

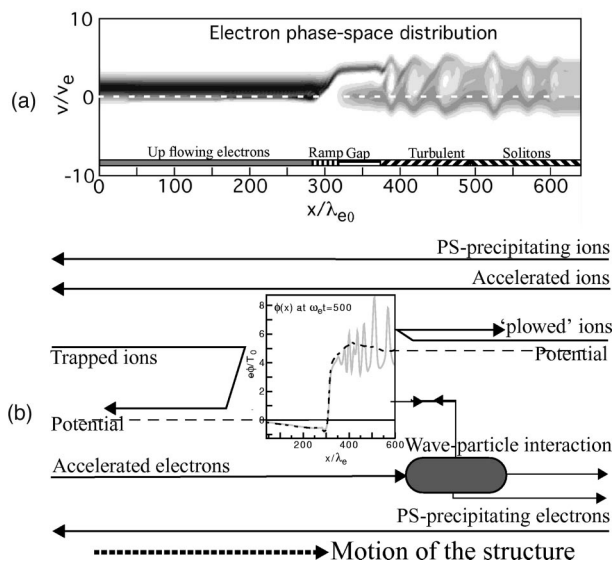


FIG. 8. Part (a) is from the numerical simulation of Ref. 36. The plot is the electron phase-space distribution at a time when a well-defined double layer has formed. Part (b) is an illustration of observed particle populations at the double layer. Inserted in the center of the illustration are the potential field from the simulation. Both the instantaneous value (solid line) and the filtered value (dashed line) are presented. The vertical distance from the potential line (dashed line) represents the particle's absolute energy (not to scale), with ions on the upper side and electrons in the lower. Particle directions are indicated by arrows.

small density depression in the presence of a current maintained through boundary injection. The ion to electron mass ratio (M_i/m_e) in the simulation is 400.

The simulation starts with ions drifting to the left at the ion thermal speed (v_i) and the electrons drifting to the right at v_e . Thus, the initial electron and ion drifts satisfy both the Bohm and Langmuir conditions and are stable to Buneman-type instabilities (Ref. 35 and references therein). The boundaries of the simulation are open, allowing the potentials at the ends of the simulation domain to float providing a more realistic representation of the observations. Figure 8(a) is in the rest frame of the double layer, that is, moving relative to the ions at the ion acoustic speed. The scale used in the simulation result is in units of the initial Debye length, rather than a time-dependent local Debye length.

Early in the simulation, an instability arises that results in electron phase-space holes (they appear as vortices in the phase-space diagrams) that move to the right.^{35,36} Later, the initial density depression evolves into a large density depression of narrow scale size and a double layer is formed. Electrons are accelerated by the net potential drop of the double layer and form a beam. This beam interacts with the stagnating downstream electrons and continues to form a series of electron phase-space holes. The plot in Fig. 8(a) is from the run described in Ref. 36 during a quasi-steady-state period, after a well developed strong double layer has been formed. The electron distribution shows a rapid thermalization after acceleration by \mathbf{E}_{\parallel} [Fig. 8(a)].

One can immediately determine that the evolved state of the simulation³⁶ [Fig. 8(a)] is qualitatively similar to the observations (Fig. 1). Properly scaled, the width of the double layer (i.e., the ramp) is determined to be $\sim 10\lambda_D$. The den-

sity depletion inside the \mathbf{E}_{\parallel} structure is $\sim 80\text{--}90\%$. On the low-potential side, the up-flowing electrons are nearly undisturbed. Ions (not shown) are accelerated through the double layer, from the high-potential side to the low-potential side. On the high-potential side, electrons are accelerated into a beam. The increase in electron velocity between the up-flowing electrons and the beam is of the order of 4 to 5 times. Intense electrostatic turbulence is found spatially separated from the double layer (the ramp). The unstable electron beam is found in the gap between the ramp and the turbulence region. The electrostatic turbulence creates electron phase-space holes that are traveling in the same direction as the electrons. The electric field amplitudes qualitatively also agree. Finally, the right-hand side of the simulation exhibits a strongly increased electron temperature with a drift (v_d) such that $v_d/v_e \sim 0.2$, this value is consistent with FAST observations during times when electron phase-space holes are observed.²⁹ From the observation, sweep S3e, this ratio is slightly higher.

Figure 8(b) presents an instantaneous potential value (solid line) together with a filtered value (dashed line) from the simulation result of Fig. 8(a). Due to the intense turbulence, the time averaged potential shape on the high-potential side (right) is difficult to determine. Interestingly, the simulation indicates a small overshoot on each side of the double layer. The measured upward ion fluxes on the high-potential side of the \mathbf{E}_{\parallel} structure, observed in sweep S2i, would be in the simulation result at the scale distance of $\sim 500\lambda_D$ [Fig. 8(a)] where the broad overshoot of the double layer is found [Fig. 8(b)]. The overshoot in the simulation supports the idea that the upward ions can be reflected and remain in front of the \mathbf{E}_{\parallel} structure.

VI. DISCUSSION

The event presented shows that a strong \mathbf{E}_{\parallel} (~ 1 V/m) exists in space plasmas confined to a narrow region tens of Debye length wide (Fig. 1). This \mathbf{E}_{\parallel} structure can be described as a strong double layer, which is a part of a larger diverging potential structure (the illustration on the right-hand side of Fig. 1). This observed double layer is moving up the field line (Fig. 2) in the same direction as the accelerated electron beam (S3e).

An illustration of the observed particle populations at the double layer is summarized in Fig. 8(b). The left-hand side is the low-potential side of the double layer (the earthward side) and the right-hand side is the high-potential side (the anti-earthward side). Electron and ion paths are shown below and above, respectively. The extended dashed line represents the potential. The vertical distance from the extended dashed line indicates the absolute energy of the particles (not to scale) and the direction of motion is indicated by arrows. The plasma sheet precipitating electrons and ions (entering from the right-hand side) are decelerated or accelerated through the double layer, respectively, and experience only a small change in energy.

Ions on the high-potential side with almost no velocity with respect to the moving double layer, such as some of the ions in the ion conic population, can be reflected by the

overshoot on the high-potential side. In the satellite reference frame these ions, which moved more or less with the same speed as the double layer, will be observed as upward ions. The ions moving in front of the double layer are not trapped, but instead plowed in front of the double layer, and are referred to as plowed ions [Fig. 8(b)]. The plowed ions are a small particle population with a minor density contribution. The population is exposed to a strong $\mathbf{E}_\perp \times \mathbf{B}$ drift which must lead to a strong perpendicular motion.

Ions that are moving downward with respect to the double layer and that have sufficient energy to pass through the overshoot will be accelerated through the double layer and be detected on the low-potential side as an accelerated ion beam (S4i), labeled accelerated ions in Fig. 8(b). Trapped ion conics are found on the low-potential side of the moving double layer [left-hand side in the Fig. 8(b)]. These ions originate from the low-potential side and have parallel velocities greater than the speed of the double layer. As ions reach the double layer they are reflected and decelerated by \mathbf{E}_\parallel . As a result, the ion conics are trapped between their mirror points and the upward moving double layer. The ion conics have the same pitch angle distribution as pressure cooked ions.³⁹ For an ion population that is heated in a limited vertical region, the pitch angle distribution of an ion conic distribution will be independent of energy (all energies will have the same pitch angles, seen in S1i). The pitch angle distribution of trapped ion conics, however, depends on the particle energy; higher energies will be closer to 90 degrees. Such pitch angle distributions are seen in S4i.

The speed of the double layer is far less than the electron thermal speed, so the motion of the double layer is negligible when analyzing the electron distributions. The current-carrying electrons are moving up the field line; as they enter the low-potential side of the double layer they are accelerated into an electron beam (S3e). The accelerated electron distribution is strongly unstable, resulting in intense electrostatic turbulence. The wave-particle interactions rapidly—within hundreds of Debye lengths local distance—stabilize the electron distribution transforming the kinetic energy of the electron beam into thermal energy. One part of the heated electron distribution on the high-potential side moves back toward the double layer [Fig. 8(b)] and is reflected at the double layer. These heated and then reflected electrons have energies below the beam energy in the electron phase-space distribution. The low-energy electron population affects and links the wave activity and the double layer. The interaction between the double layer and the electrostatic wave turbulence has been observed,³⁵ but a detailed understanding is a task for future studies.

Formation of \mathbf{E}_\parallel in the downward current region was discussed in Ref. 40 where it is argued that the decreasing ionospheric plasma density with altitude and a strong current density under the principle of quasineutrality leads to electron acceleration. The downward current is carried by upward moving electrons. As the gravitationally bound ion density drops with increasing altitude, the electron density must also decrease to maintain quasineutrality in each flux tube. Hence, the electrons drift velocity (upward) must increase to maintain the current. If the current density is strong or the

ambient ion density is weak, the electrons may be accelerated to many times their initial thermal speed. Such a scenario fits well with the double layer formation seen in the simulation.

Ion heating may play a strong role by increasing the ion density at high altitudes. The heated ions will slowly increase their parallel velocity due to the magnetic field topology, forming ion conics. The moving double layers (at the ion acoustic velocity) force the ion conics (on the low potential side) to have a parallel velocity less than or equal to the local ion acoustic velocity. Thus, the speed of the ion conics is controlled by the double layer and they cannot continuously increase their speed. The double layers also offer a source of waves on the high-potential side that can heat ions. The moving double layer's impact on the ions has not previously been clearly investigated. The observations in this paper indicate that the acceleration process needs to be re-evaluated in the context of how ion conics effect or are effected by double layers.

It is possible that multiple double layers may be present on the same magnetic flux tube. In such a case, electrons are accelerated in steps by each double layer with particle distribution relaxation in between (transforming the gained kinetic energy from the double layer into thermal energy) and ion flow is controlled by the double layers. This scenario has some support in the observations. In the event above, the electrons on the low-potential side appear to already have experienced some acceleration (50 eV). Electron acceleration through the double layers is seen to be $4-5v_e$ in both observations and simulations. Thus, the strongly accelerated electron populations (~ 1000 eV) from a cold (~ 1 eV) source would require four such double layers, each with geometrically increasing potential.

VII. SUMMARY

A parallel electric field has been observed in the downward current region by the FAST satellite. For the first time, a double layer has been studied in detail with both electric field and particle measurements. The upward electron and downward ion beams and the integrated \mathbf{E}_\perp all indicate the same parallel potential. The inferred velocity of the \mathbf{E}_\parallel structure is equal to that of the detected upward plowed ion fluxes as well as the local ion acoustic speed. This velocity also agrees within the observational uncertainties with the calculated velocity delay times of the \mathbf{E}_\parallel structure on the probes. The size and velocity of the \mathbf{E}_\parallel structure are measured by different instruments with the quantities in agreement.

The observation and the numerical simulation are also in good agreement. The observed \mathbf{E}_\parallel structure can be well described as a strong double layer. The small scale features can be understood from the simulation, but some details need further investigation.

The parallel electric field is confined to a thin layer, about 10 Debye lengths, moving upward at approximately the speed of the ion acoustic velocity. Electrons are accelerated by the double layer to several times their initial thermal energy (Table I and Fig. 8). The accelerated electron population—a beam distribution—is strongly unstable and

results in intense electrostatic turbulence. The wave turbulence is not observed at the double layer and in fact, the electrostatic wave turbulence region is spatially separated from the double layer. The wave turbulence displays clear signatures of electron phase-space holes hundreds of Debye lengths from the double layer. The intense wave turbulence rapidly plateaus the electron distribution (Figs. 6 and 7).

A double layer is highly dynamical and interacts with all charged particle populations. In light of these new observations the large scale effect of acceleration needs to be reinvestigated. For instance, on a flux tube with a double layer the parallel velocity of ion conics will be constrained and the ionospheric–magnetospheric currents will hence be effected.

ACKNOWLEDGMENTS

This research was supplied by the Fast Auroral Snapshot data analysis program Grant No. NAG5-3596 and NASA program Grant No. NAG5-9353.

- ¹D. M. Klumpar and W. J. Heikkila, *Geophys. Res. Lett.* **9**, 873 (1982).
- ²J. L. Burch, P. H. Rieff, and M. Sugiura, *Geophys. Res. Lett.* **10**, 753 (1983).
- ³B. Hultqvist, R. Lunding, K. Stasiewicz *et al.*, *J. Geophys. Res.* **93**, 9765 (1988).
- ⁴M. H. Boehm, J. Clemmons, J.-E. Wahlund, A. Eriksson, L. Eliasson, L. Blomberg, P. Kintner, and H. Höfner, *Geophys. Res. Lett.* **22**, 2103 (1995).
- ⁵W. Miyake, T. Mukai, and N. Kaya, *Ann. Geophys.* **16**, 940 (1998).
- ⁶R. D. Sharp, E. G. Shelley, R. G. Johnson, and A. G. Ghielmetti, *J. Geophys. Res.* **85**, 92 (1980).
- ⁷C. S. Lin, J. L. Burch, J. D. Menietti, and R. A. Hoffman, *Geophys. Res. Lett.* **9**, 925 (1982).
- ⁸J. P. McFadden, C. W. Carlson, and R. E. Ergun, *J. Geophys. Res.* **104**, 14453 (1999).
- ⁹C. W. Carlson, J. P. McFadden, R. E. Ergun *et al.*, *Geophys. Res. Lett.* **25**, 2017 (1998).
- ¹⁰H. L. Collin, R. D. Sharp, and E. G. Shelley, *J. Geophys. Res.* **87**, 7504 (1982).
- ¹¹B. Hultqvist, *Planet. Space Sci.* **19**, 749 (1971).
- ¹²J. D. Winningham, J. L. Burch, and R. A. Frahm, *J. Geophys. Res.* **89**, 1751 (1984).
- ¹³G. Marklund, L. Blomberg, C.-G. Fälthammar, and P.-A. Lindqvist, *Geophys. Res. Lett.* **21**, 1859 (1994).
- ¹⁴R. E. Ergun, C. W. Carlson, J. P. McFadden *et al.*, *Geophys. Res. Lett.* **25**, 2025 (1998).
- ¹⁵R. C. Elphic, J. W. Bonnell, R. J. Strangeway *et al.*, *Geophys. Res. Lett.* **25**, 2033 (1998).
- ¹⁶R. C. Elphic, J. Bonnell, R. J. Strangeway, C. W. Carlson, M. Temerin, J. P. McFadden, R. E. Ergun, and W. Peria, *Geophys. Monog.* 118, edited by S.-I. Ohtani *et al.* (American Geophysical Union, Washington, DC, 2000), p. 173.
- ¹⁷F. S. Mozer, C. A. Cattell, M. K. Hudson, R. L. Lysak, M. Temerin, and R. B. Torbert, *Space Sci. Rev.* **27**, 155 (1980).
- ¹⁸M. Temerin, K. Cerny, W. Lotko, and F. S. Mozer, *Phys. Rev. Lett.* **48**, 1175 (1982).
- ¹⁹F. S. Mozer and C. A. Kletzing, *Geophys. Res. Lett.* **25**, 1629 (1998).
- ²⁰R. E. Ergun, Y.-J. Su, L. Andersson *et al.*, *Phys. Rev. Lett.* **87**, 045003 (2001).
- ²¹J. S. DeGroot, C. Barnes, A. E. Walstead, and O. Buneman, *Phys. Rev. Lett.* **38**, 1283 (1977).
- ²²S. Iizuka, K. Saeki, N. Sato, and Y. Hatta, *Phys. Rev. Lett.* **43**, 1404 (1979).
- ²³N. Singh and R. W. Schunk, *Geophys. Res. Lett.* **9**, 1345 (1982).
- ²⁴H. Schamel and S. Bujarbarua, *Phys. Fluids* **26**, 190 (1983).
- ²⁵H. Matsumoto, H. Kojima, T. Miyatake, Y. Omura, M. Okada, I. Nagano, and M. Tsutsui, *Geophys. Res. Lett.* **21**, 2915 (1994).
- ²⁶F. S. Mozer, R. E. Ergun, M. Temerin, C. Cattell, J. Dombek, and J. Wygant, *Phys. Rev. Lett.* **79**, 1281 (1997).
- ²⁷R. E. Ergun, C. W. Carlson, J. P. McFadden *et al.*, *Geophys. Res. Lett.* **25**, 2041 (1998).
- ²⁸R. E. Ergun, C. W. Carlson, J. P. McFadden, F. S. Mozer, L. Muschietti, I. Roth, and R. J. Strangeway, *Phys. Rev. Lett.* **81**, 826 (1998).
- ²⁹R. E. Ergun, C. W. Carlson, L. Mushetti, I. Roth, and J. P. McFadden, *Nonlinear Processes in Geophysics* **6**, 187 (1999).
- ³⁰M. V. Goldman, M. M. Oppenheim, and D. L. Newman, *Geophys. Res. Lett.* **26**, 1821 (1999).
- ³¹T. Miyake, Y. Omura, and H. Matsumoto, *J. Geophys. Res.* **105**, 23239 (2000).
- ³²N. Singh, S. M. Loo, B. E. Wells, and C. Deverapalli, *Geophys. Res. Lett.* **27**, 2469 (2000).
- ³³M. M. Oppenheim, G. Vetoulis, D. L. Newman, and M. V. Goldman, *Geophys. Res. Lett.* **28**, 1891 (2001).
- ³⁴L. Mandrake, P. L. Pritchett, and F. V. Coroniti, *Geophys. Res. Lett.* **27**, 2869 (2000).
- ³⁵D. L. Newman, M. V. Goldman, R. E. Ergun, and A. Mangeney, *Phys. Rev. Lett.* **87**, 255001 (2001).
- ³⁶M. V. Goldman, D. L. Newman, and R. E. Ergun, *Nonlinear Processes in Geophysics* (in press).
- ³⁷C. W. Carlson, R. F. Pfaff, and J. G. Watzin, *Geophys. Res. Lett.* **25**, 2013 (1998).
- ³⁸C. W. Carlson, J. P. McFadden, P. Turin, D. W. Curtis, and A. Magoncelli, *Space Sci. Rev.* **98**, 33 (2001).
- ³⁹D. J. Gorney, Y. T. Chiu, and D. R. Croley, Jr., *J. Geophys. Res.* **109**, 4205 (1985).
- ⁴⁰M. Temerin and C. W. Carlson, *Geophys. Res. Lett.* **25**, 2365 (1998).